Journal of Solid State Chemistry **160,** 123–133 (2001)
doi:10.1006/jssc.2001.9204, available online at http://www.idealibrary.com on IDEAL®

Charge-Carrier Localization on Mn Surface Sites in Granular $LaMnO_{3+\delta}$ Samples

I. Maurin,[1] P. Barboux, Y. Lassailly, and J.-P. Boilot

Laboratoire de Physique de la Matière Condensée, CNRS UMR C7643, Ecole Polytechnique, 91128 Palaiseau, France

F. Villain

Laboratoire de Chimie Inorganique et Matériaux Moléculaires, CNRS ESA 7071, Université Pierre et Marie Curie, 4 place Jussieu, 75232 Paris Cedex 05, France

and

P. Dordor

Institut de Chimie de la Matière Condensée de Bordeaux, CNRS UPR 9048, Université Bordeaux I, 87 Avenue du Dr. A. Schweitzer, 33608 Pessac, France

Received December 21, 2000; in revised form March 29, 2001; accepted April 9, 2001; published online July 6, 2001

Mn *K*-edge X-ray absorption experiments have been carried out on the self-doped $LaMnO_{3+\delta}$ system and compared to a $(La_{1-x}Ca_x)MnO_3$ reference series. For both systems, the absorption edge and the unit cell volume vary linearly with the formal Mn(IV) content, indicating a direct correlation between the hole count in Mn 3*d* states and the concentration of substituents or cationic vacancies in the perovskite structure. However for the $LaMnO_{3+\delta}$ system, a deviation from linearity occurs in the volume change at high δ values. This discontinuity is ascribed to a limit of solubility for the cationic vacancy insertion, evidenced for 30% of Mn(IV). Larger hole contents can still be measured in samples synthesized at low temperature and showing a small grain size, but these excess holes are then localized on Mn surface sites. Based on resistivity and thermopower measurements, the differences in hole doping through aliovalent substitution or vacancy insertion are discussed, highlighting the existence of a large ferromagnetic insulating composition range in the $LaMnO_{3+\delta}$ system for $0.1 \leq \delta \leq 0.15$.

Key Words: **lanthanum manganites; nonstoichiometry; electronic localization; thermopower; X-ray absorption spectroscopy.**

INTRODUCTION

The electronic properties of manganite perovskite oxides have potential applications in catalysis, as active material for hydrocarbon oxidation or as an electrode in solid oxide fuel cells (1), and in magnetic recording as magnetoresistant reading heads (2, 3). Hole doping the antiferromagnetic insulator $LaMnO_3$ strongly modifies its electrical and magnetic properties. The hole-doped compounds undergo a paramagnetic-to-ferromagnetic transition upon cooling, which is accompanied by a sharp decrease in resistivity (3, 4). In such systems, correlations between the magnetic and transport properties have been qualitatively explained by the double-exchange model (5), as resulting from a mixed-valence state Mn^{3+}–Mn^{4+}. The number of mobile carriers can then be tuned continuously either by aliovalent substitution of La(III) by elements A of lower valence, $(La_{1-x}A_x)MnO_3$, or by an oxygen overstoichiometry, $LaMnO_{3+\delta}$.

Lanthanum manganites exhibit a wide range of oxidative nonstoichiometry, at first written as $LaMnO_{3+\delta}$ (6). Actually, oxygen interstitials cannot be accommodated in the perovskite structure and the oxygen excess accounts here for cationic vacancies, as argued by van Roosmalen *et al.* (7, 8). These authors suggested equal amounts of La and Mn vacancies to model the defect chemistry in this system. As a consequence, written as $La_{3/(3+\delta)}Mn_{3/(3+\delta)}O_3$ would be more appropriate. Nevertheless, we will still refer in this paper to the $LaMnO_{3+\delta}$ notation for the sake of simplicity. Hereafter, we will use the term of formal Mn(IV) content ($Mn(IV) = 2\delta$), which accounts for the hole density as compared to stoichiometric $LaMnO_3$, instead of Mn^{4+} concentration. Indeed, the charge compensation that requires the vacancy insertion can affect the O 2*p* occupancy by analogy with Cu-based superconductors (9), as well as the Mn 3*d* count. Moreover, the point defects can induce localized

[1] Present address: Fullerene Science Center, CPES University of Sussex, Falmer, Brighton BN1 9QJ, United Kingdom.

0022-4596/01 $35.00

states, corresponding for instance to oxygen dangling bonds surrounding a Mn vacancy.

The oxygen overstoichiometry can be increased by annealing, at low temperature (10–17) or under high oxygen partial pressures (14, 16), or alternatively by electrochemical oxidation at room temperature (18). However, the $LaMnO_{3+\delta}$ phases cannot be oxidized higher than $\delta = 0.15 \pm 0.01$ using annealing procedures in air (10–16). This value appears to be the upper limit for the cationic vacancy insertion simultaneously on the La and Mn sites. Nevertheless, higher Mn oxidation states, up to $\delta = 0.20$, can be obtained through direct crystallization of the perovskite phase at low temperature (11, 12, 17). Note that for the particular $LaMnO_{3.15}$ composition, showing vacancy contents as high as 5% on each cationic site, no clustering effects between the ionic defects were detected by high-resolution transmission electron microscopy (7).

As observed in the aliovalent-doped systems, the antiferromagnetic state in stoichiometric $LaMnO_3$ evolves toward a ferromagnetic long-range order in the $LaMnO_{3+\delta}$ series when $\delta \geq 0.05$. However, the ferromagnetic compounds remain insulators and a low-temperature metal-like conductivity is only observed for $\delta > 0.15$ (11, 12, 14, 17). This persistence of an insulating behavior at high hole-doping levels may result from a decrease in the density and/or mobility of the charge-carriers. Indeed, vacancies, especially those on the Mn sites, induce stronger site-binding energies than an aliovalent substitution. Besides, a break in the regular periodicity of the crystal and electrostatic interactions between holes and charged defects may decrease the carrier mobility and lead to an Anderson-type localization. On the other hand, at high vacancy concentrations, the orbitals related to the oxygen dangling bonds may overlap, forming a defect band and, according to Mott criterion, giving rise to metallic conduction.

In order to have a better understanding of the mechanisms that drive differences in hole doping either by chemical substitution or by insertion of cationic vacancies, we report an investigation of the structural, magnetic, and transport properties of $LaMnO_{3+\delta}$ phases over a wide range of nonstoichiometry, $0.03 \leq \delta \leq 0.21$. Comparison is made with a compilation of literature data and with a $(La_{1-x}Ca_x)MnO_3$ reference series. This latter system presents a crystallographic structure similar to that of the self-doped series, on account of the similarity between Ca^{2+} and La^{3+} ionic radii, respectively 1.34 and 1.36 Å in 12-fold coordination (19). The assumption of a charge-carrier localization is discussed in the light of X-ray absorption spectroscopy (XAS) and Seebeck measurements.

EXPERIMENTAL

$(La_{1-x}Ca_x)MnO_3$ $(0.08 \leq x \leq 1)$ and $LaMnO_{3+\delta}$ $(0.03 \leq \delta \leq 0.21)$ polycrystalline samples were synthesized using a method derived from the citrate-ethyleneglycol process (20). The Ca-doped series, used as a reference, was prepared at high temperature (1400–1475°C) in order to avoid the vacancy formation. In the case of the $LaMnO_{3+\delta}$ series, the cationic vacancy concentration was controlled by the synthesis temperature. After calcination of the citrate-ethyleneglycol resin at 400°C, the amorphous powders were ground, pressed into pellets, and sintered in air at various temperatures, 600–1475°C, for 18 to 60 h. Kinetic studies have shown that these heating times are sufficient to reach the full crystallization of the perovskite phase, so that no residual amorphous phase was present in the final materials. For such a study, a solution method was essential to warrant high homogeneity in the cation distribution, especially in the case of low-temperature syntheses. The samples heat-treated below 1000°C were quenched at room temperature in order to overcome species diffusion during cooling. The La/Mn ratio (0.99 ± 0.01) was measured by inductive coupled plasma emission spectroscopy and the total oxygen content, δ was estimated by iodometric titration with an accuracy of 0.01. Results are reported in Table 1. The samples were characterized by X-ray diffraction (XRD) using a *Philips MPD X-Pert* diffractometer equipped with

TABLE 1
Synthesis Temperature, Formal Mn(IV) Content, Lattice Parameters, and Unit Cell Volume (per Formula Unit) for the $(La_{1-x}Ca_x)MnO_3$ Samples $(0.08 \leq x \leq 1)$

$(La_{1-x}Ca_x)MnO_3$ x	Synthesis temperature (°C)	Mn(IV) content (%)	a (Å)	b (Å)	c (Å)	Unit cell volume (Å^3)
0.08	1475	17±2	5.530	7.731	5.603	59.88±0.02
0.2	1400	26±2	5.492	7.764	5.504	58.68±0.03
0.33	1475	34±2	5.472	7.711	5.457	57.56±0.02
0.4	1400	41±2	5.441	7.682	5.454	56.99±0.03
0.5	1400	50±2	5.418	7.640	5.426	56.16±0.02
0.6	1400	61±2	5.400	7.599	5.397	55.37±0.02
0.8	1400	79±2	5.3342	7.536	5.337	53.64±0.02
1	1400	94±2	5.268	7.458	5.284	51.89±0.03

TABLE 2

Synthesis Temperature, Formal Mn(IV) Content, Lattice Parameters, Unit Cell Volume (per Formula Unit), Grain Size Determined by Electron Microscopy, and Coherence Length of the Diffraction Domains for the $LaMnO_{3+\delta}$ samples ($0.03 \leq \delta \leq 0.21$)

$LaMnO_{3+\delta}$ δ	Temp. (°C)	Mn(IV) content (%)		a (Å)	b (Å) or α (°)	c (Å)	Unit cell volume (Å^3)	Grain size nm (TEM)	Coherence domains X-ray (nm)
0.03	1475	7±2	O	5.538	7.704	5.719	61.00±0.02	~10000	n.a.
0.05	1350	10±2	0 + R	5.538	7.731	5.650	60.47±0.03		n.a.
0.07	1200	15±2	0 + R	5.537	7.795	5.502	59.37±0.03		n.a.
0.09	1100	19±2	R	5.479	60.68		59.04±0.04	1000	n.a.
0.10	1000	21±2	R	5.482	60.66		59.04±0.05	700	
0.13	1000	26±2	R	5.480	60.61		58.97±0.06	500	450
0.15	900	30±2	R	5.474	60.64		58.83±0.04	90	85
0.18	750	36±2	R	5.473	60.54		58.67±0.04	35	45
0.19	700	38±2	R	5.467	60.52		58.45±0.08	30	
0.21	600	42±2	R	5.466	60.51		58.42±0.08	25	30

Note. O, orthorhombic; *R*, rhombohedral. When two phases are present, only the lattice parameters of the majority one are listed. The grain size is estimated with an accuracy of 10%. The coherence length of the crystallites, *D*, is determined from the width of the diffraction peak at $2\theta \sim 46.7°$ using the Scherrer formula and assuming a spherical shape for the domains.

a Cu anode. The diffraction patterns were analyzed by means of Rietveld treatment or least-squares refinement of the Bragg positions to extract the lattice parameters. The $LaMnO_{3+\delta}$ samples present a rhombohedral structure ($R\bar{3}c$ space group) when $\delta \geq 0.09$. The $LaMnO_{3.05}$ and $LaMnO_{3.07}$ compositions show an orthorhombic (*Pnma*) majority phase with traces of the rhombohedral form, as observed by other authors (12). This latter phase may come from a partial reoxidation during cooling. Only the $LaMnO_{3.03}$ sample is purely orthorhombic (Table 1).

Observations by transmission electron microscopy show that reactions at low temperatures (e.g., 600°C) lead to very small grain sizes (approx. 25 nm in diameter). These small sizes coincide with the length of the coherence domains obtained from the width of the X-ray diffraction peaks (Table 2).

The X-ray absorption experiments were performed at the Laboratoire pour l'Utilisation du Rayonnement Electromagnétique (LURE) on the DCI synchrotron radiation storage ring. The XAS data were collected at the Mn *K*-edge on the D42 beam line using a Si (311) double-crystal monochromator. Rejection of the harmonics was achieved by a slight detuning of the parallelism of the two crystals. Experiments were carried out in the transmission mode with air-filled ionization chambers. Appropriate amounts of powder were diluted in cellulose to optimize the edge jump. The X-ray absorption near edge structure (XANES) spectra were recorded in the energy range 6520–6640 eV, per steps of 0.3 eV. A metallic manganese foil, simultaneously measured, was used as an energy standard (energy of the first inflection point taken as 6539.0 eV). The background was subtracted by fitting the pre-edge region with a linear function, and the absorption spectra were normalized at the inflection point of the first XAFS oscillation (approx. 6564 eV). This latter procedure was validated by analyzing XANES spectra of mixtures of manganite samples showing different Mn oxidation states: $LaMnO_{3.03}$ (Mn(IV) = 6%) + $(La_{0.2}Ca_{0.8})MnO_3$ (Mn(IV) = 79%) and $LaMnO_{3.03}$ + $LaMnO_{3.15}$ (Mn(IV) = 30%). These spectra were reproduced by curves calculated as the sum of the spectra of the different manganite components. The quality of the simulation depends on the normalization point. Only the procedure described above gives good results for all the mixtures. Some examples of these simulations are reported in Ref. (21).

The magnetic and transport properties were investigated as a function of the Mn valence state in the $LaMnO_{3+\delta}$ and $(La_{1-x}Ca_x)MnO_3$ systems. Electrical resistivity measurements were carried out between 5 and 300 K using a standard four-probe technique. Metal-to-insulator transitions (T_ρ) were determined as the maximum of the resistivity curves. Dc magnetizations were measured with a SQUID magnetometer. Curie temperatures (T_C) were defined as the inflection point of magnetization versus temperature curves, recorded under a field of 1000 Oe. The saturation magnetization, M_{sat}, was determined from hysteresis loops at 5 K with an accuracy of approx. 0.04 μ_B/Mn. M_{sat} roughly corresponds to the magnetization under 5 T. Thermopower measurements were carried out at the ICMCB using homebuilt devices (22). The samples were suspended between electrically isolated posts, copper posts for the low-temperature (LT) cell (6–300 K) and gold posts for the high-temperature (HT) cell (100–525 K). For the LT experiments, the Seebeck coefficient α was measured by a conventional differential method. α was determined as relative to

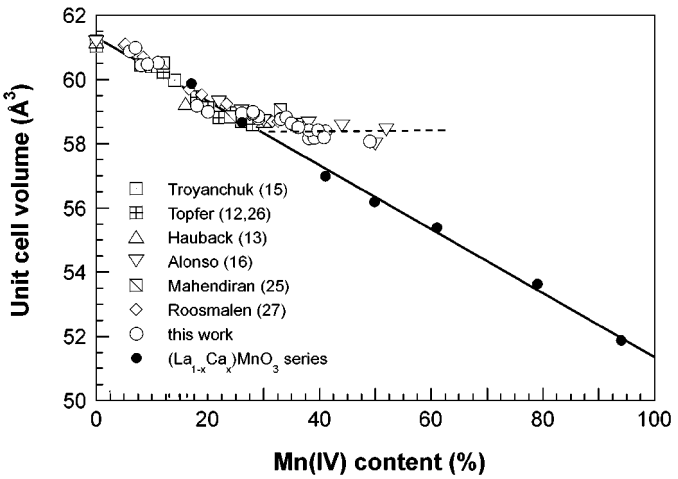

FIG. 1. Variation of the unit cell volume (per formula unit) as a function of the formal Mn(IV) content for the two series, $(La_{1-x}Ca_x)MnO_3$ (full circles) and $LaMnO_{3+\delta}$ (open symbols).

copper using a chromel–Cu–Fe reference thermocouple. In the HT cell, the thermal gradient was measured using Pt resistances.

RESULTS AND DISCUSSION

Evidence for Charge-Carrier Localization

The $(La_{1-x}Ca_x)MnO_3$ ($0.08 \leq x \leq 1$) phases heat-treated at 1400°C are nearly stoichiometric, except for the lowest Ca^{2+} contents, so that their Mn(IV) count corresponds to x. The choice of Ca, as a substituent for La, leads to orthorhombic structures (*Pnma* space group) over the whole range of doping (23). The lattice parameters and unit cell volume of the different samples are listed in Table 1. The unit cell volume V gradually decreases from $LaMnO_3$ to $CaMnO_3$ (Fig. 1). Thus, V follows a simple linear variation as a function of the formal Mn(IV) (or Ca^{2+}) content. This is in agreement with Vegard law. The linear volume change is independent of the cell symmetry and follows

$$V\ (\text{Å}^3) = 61.03 - 0.096.y, \qquad [1]$$

where y denotes the Mn(IV) percentage.

The volume ratio between La^{3+} and Ca^{2+}, less than 2%, cannot explain this 16% change in the unit cell volume. Moreover, when La is substituted by other cations either divalent or monovalent such as Sr^{2+} and Na^+, the cell volume still follows Eq. [1]. Yet, Na^+ and Sr^{2+} are larger than La^{3+} in 12-fold coordination. The ionic radius of La^{3+} is 1.36 Å while it is 1.39 Å for Na^+ and 1.44 Å for Sr^{2+} (19). This means that the decrease in the lattice volume from $LaMnO_3$ to $CaMnO_3$ is primarily caused by the decrease in Mn–O bond length, which results from the Mn 3*d* band depleting upon doping. Consequently, the unit cell volume is quite insensitive to the crystal symmetry and to changes in the Mn–O–Mn angle, contrary to the magnetic and transport properties (24). Note, however, that Eq. [1] is not valid for substituents of much larger ionic radius such as Ba^{2+} (1.64 Å in 12-fold coordination). In that case, the lattice volume is no longer determined by the Mn–O bond length.

The structural parameters of our $LaMnO_{3+\delta}$ samples are reported in Table 2. We have compiled various literature data (13, 15, 16, 25–27) in addition to ours in order to check whether the previous variation of the unit cell volume with the Mn valence state is relevant for the self-doped system. Figure 1 shows that Eq. [1] still fits the experimental data for the low vacancy concentrations, $\delta \leq 0.15$. However, a deviation from the linear behavior is observed by all authors above 30% of Mn(IV), i.e., 5% of vacancies on each cationic site. The good reproducibility of the various data provides a precise determination of the vacancy threshold, above which the unit cell volume remains constant. This deviation could be first attributed to a size effect of the cationic vacancies. For this to occur, their presence should enlarge the crystal lattice, but in that case, one would expect a gradual deviation from the linear behavior instead of a sharp break. Therefore, this volume discontinuity rather evidences a limit of solubility for pairs of La and Mn vacancies.

As XRD patterns do not show any secondary phase above this solubility limit, the samples may be described as a 30% hole-doped phase with excess holes trapped in the vicinity of cationic vacancies. Surface sites may also be involved in the trapping process since Mn(IV) contents higher than 30% are observed in finely divided materials (Table 2). In order to check the assumption of a charge-carrier localization, we have analyzed Mn *K*-edge XAS measurements performed on the two series, $(La_{1-x}Ca_x)MnO_3$ and $LaMnO_{3+\delta}$.

The normalized XANES spectra of the calcium and vacancy-doped samples are presented in Figs. 2 and 3 respectively. Each spectrum shows a pre-edge structure (labeled A) related to $1s \rightarrow 3d$ transitions allowed by (i) quadrupolar effects and (ii) a covalent mixing between Mn 3*d* and 0 2*p* states (28), then a main absorption line, B, which arises from transitions to Mn 4*p* bonded states and a near post-edge region (labeled C). In the latter, the X-ray absorption is generally modulated by multiple scatterings of the photoelectron on atoms surrounding the absorbing site. Hereafter, we will focus on the main line, B, whose shape strongly depends on the symmetry of the $[MnO_6]$ moiety. In the case of binary oxides, e.g., Mn_2O_3 and MnO_2, different types of Mn coordination shells (distorted octahedra and trigonal prisms) lift the degeneracy of the $4p_{x,y,z}$ levels and induce the splitting of the $1s \rightarrow 4p$ transitions (29, 30). For the manganite perovskite oxides, the spread of the Mn–O distances remains narrow enough (30) and yields an unresolved main

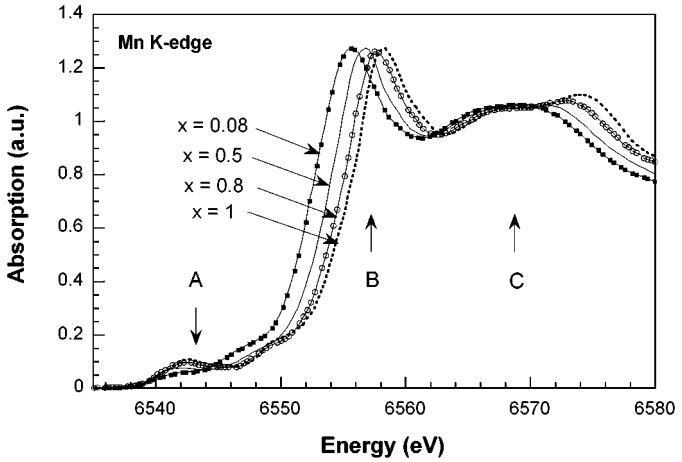

FIG. 2. Normalized Mn *K*-edge spectra recorded at room temperature for the $(La_{1-x}Ca_x)MnO_3$ series, $x = 0.08$, 0.5, 0.8, and 1.

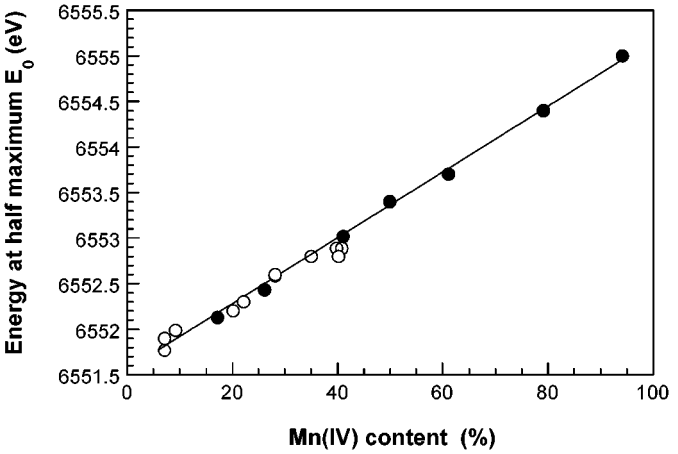

FIG. 4. Energy of the main absorption line at half maximum, E_0, as a function of the formal Mn(IV) content for the two series, $(La_{1-x}Ca_x)MnO_3$ (full circles) and $LaMnO_{3+\delta}$ (open circles). The reproducibility of the monochromator position allowed us to measure absorption edge shifts of less than 0.1 eV.

line even for the compositions showing strong Jahn–Teller distortions (Fig. 2).

In the $(La_{1-x}Ca_x)MnO_3$ series, the absorption edge is shifted to high energies when the Ca^{2+} content increases, as previously reported (29, 31, 32). This energy displacement is first ascribed to an increase in 1*s* core state binding energy, associated with the decrease in the screening effects when removing a 3*d* electron. It also accounts for a larger overlap between Mn 4*p* and O 2*p* orbitals. This overlap, related to the decrease in Mn–O bond length when depleting the Mn 3*d* band, strongly destabilizes Mn 4*p* antibonding states and consequently increases the energy of the $1s \rightarrow 4p$ transitions. With the normalization procedure used, the intensity and the width of the main line remain slightly unchanged in the $(La_{1-x}Ca_x)MnO_3$ system. From $LaMnO_3$ to $CaMnO_3$, the absorption edge is only shifted, reflecting an average Mn oxidation state. Indeed, the experimental data cannot be reproduced by a weighted combination of $LaMnO_3$ and $CaMnO_3$ spectra, i.e., by a simple mixture of Mn^{3+} and Mn^{4+} ionic species (31, 32). Besides, the edge position, defined here as the energy of the main line at half maximum, E_0 shows a linear variation as a function of the Mn(IV) content, y (Fig. 4):

$$E_0 \text{ (eV)} = 6551.6 + 0.036.y \ (0 \leq y \leq 100). \qquad [2]$$

Such a correlation and the absence of broadening of the main line demonstrate that holes are uniformly distributed over the Mn sites.

In the $LaMnO_{3+\delta}$ system, the absorption edge is also shifted to higher energies when the Mn oxidation state increases (Fig. 3). The chemical shift ΔE_0 of the non-stoichiometric samples can still be superimposed to the line reported for the Ca-doped series (Fig. 4). This accounts for similar local Mn environments, i.e., similar Mn–O bond lengths, in the two systems. However, the main absorption line undergoes a broadening associated with a decrease in its amplitude at high Mn valence states, $\delta > 0.15$ (Fig. 3). Thus, this change occurs for the compositions that show a discontinuity in the variation of their unit cell volume. The broadening indicates unequivalent Mn sites and can be reproduced by a mixture of different absorption spectra. For instance, the decrease in the edge slope observed for the $LaMnO_{3.21}$ composition can be qualitatively modeled by a linear combination of the spectra of the two end members, $LaMnO_3$ and $CaMnO_3$, in a ratio that corresponds to the average Mn oxidation state of the sample (inset of Fig. 5).

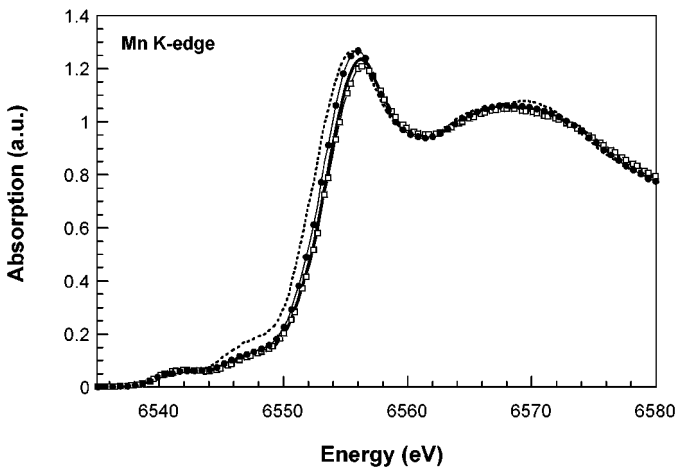

FIG. 3. Normalized Mn *K*-edge spectra recorded at room temperature for the $LaMnO_{3+\delta}$ series, $\delta = 0.03$ (– – –), 0.15 (●), 0.18 (—), and 0.21 (□).

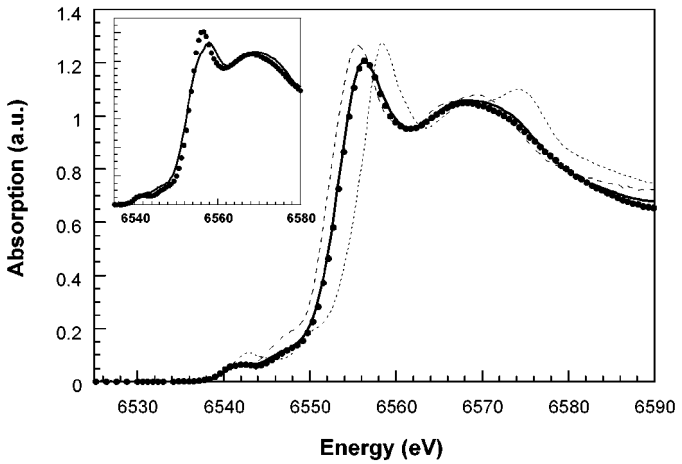

FIG. 5. Comparison between the experimental XANES spectrum of a $LaMnO_{3.21}$ sample (full circles) and a curve calculated as a combination of the spectra of $CaMnO_3$ (dotted line) and $LaMnO_{3.15}$ (dashed line) in the respective weights 17 and 83% (solid line) is made. In the inset, comparison with a curve calculated as a simple linear combination of 0.58 $LaMnO_3$ and 0.42 $CaMnO_3$ spectra (solid line) is made.

In the highly doped $LaMnO_{3+\delta}$ samples, the fact that the edge position does not deviate from Eq. [2] indicates that the holes coming from the vacancy charge compensation are distributed over Mn sites only. In particular, the vacancies do not induce localized states such as oxygen dangling bonds or color centers. However, the hole distribution over the Mn sites is not uniform any more, as evidenced by the change in the intensity of line B. The edge position cannot account for it since E_0 is not sensitive to a spread of Mn–O bond lengths, as shown by several authors from the comparison of $LaMnO_3$ and Mn_2O_3 (or $CaMnO_3$ and MnO_2) XANES spectra (29, 30). Considering now local fluctuations of the electronic density distributed between a 30% hole-doped majority phase (at the solubility limit for the cationic vacancy insertion) and domains constituted of pure Mn^{4+}, it is possible to simulate the various broadened spectra. Figure 5 compares the $LaMnO_{3.21}$ spectrum with a curve calculated by adding the spectra of $LaMnO_{3.15}$ (Mn(IV) = 30%) and $CaMnO_3$, in the respective weights of 83% and 17%. Again, the weights of the two components were deduced from the average Mn(IV) content of the sample. The main features of the experimental spectrum, both the pre-edge and main edge absorption, are reproduced without any adjustable parameters. A good agreement is also observed in the case of the $LaMnO_{3.18}$ composition. Therefore, the spectra of the highly doped $LaMnO_{3+\delta}$ samples account for two contributions: a 30% hole-doped perovskite phase containing holes delocalized among equivalent Mn^{3+} sites and Mn^{4+} species. The latter component cannot be identified with a MnO_2 segregated phase since replacing $CaMnO_3$ by MnO_2 in the simulation leads to a poor agreement. Moreover, under the synthesis conditions used, this manganese oxide would not be stable toward a reduction into Mn_2O_3. Note that the trapping process is not only limited to the time scale of the photoelectric process (10^{-15} s) since it is also observed from the diffraction studies (Fig. 1).

These localized Mn^{4+} species account for a hole trapping adjacent either to ionic vacancies or more probably to surface sites. Indeed, Mn(IV) contents higher than 30% are only obtained in nanometric powder samples (Table 2), and a rough calculation shows that about 10% of Mn sites enclosed in a spherical particle of 25 nm in diameter are located at the surface, a value on the same order as the hole count in excess of the solubility limit. Moreover, the fact that the $LaMnO_{3+\delta}$ samples synthesized at high temperature, i.e., with a large grain size, cannot be oxidized above $\delta = 0.15$ by annealing at low temperature (12) or under high oxygen partial pressure (14) is consistent with an assumption of surface sites that stabilize and trap the excess holes. Hence, the extra holes may not be associated with additional vacancies but with surface sites, which possibly correspond to an oxygen-terminated surface.

Origin of the Localization Process: A Decrease of the Carrier Mobility

Considering the role of surface sites in the trapping process, we address in the following the relationship between electronic localization and surface disorder effects in samples showing a high surface-to-volume ratio. To evidence a particular behavior of Mn surface sites in granular samples, we have performed XAS experiments on $(La_{0.67}Ca_{0.33})MnO_{3+\delta}$ compounds synthesized between 625 and 1475°C. Their grain size ranges from 25 nm to 10 μm and their vacancy concentration remains low: $\delta \leq 0.05$. Their XANES spectra do not show any decrease of the maximum absorption, indicating that surface and grain boundaries are not sufficient to ensure a hole trapping. Therefore, interactions of the charge-carriers with the ionic defects must be considered.

Influence of the charged vacancies on the carrier mobility has been clarified through combined resistivity and thermopower (TEP) experiments. This latter technique allows the determination of the activation energy of the charge-carrier density, E_S. Note that this quantity is not sensitive to microstructure effects, hence to the grain size, since no currents flow in the samples during the measurements. Results of the TEP experiments performed on the $LaMnO_{3+\delta}$ compounds are shown in Fig. 6. As previously reported for the Ca-doped series (33, 34), the Seebeck coefficient, α, in the paramagnetic regime fits a linear function of $1/T$ (inset of

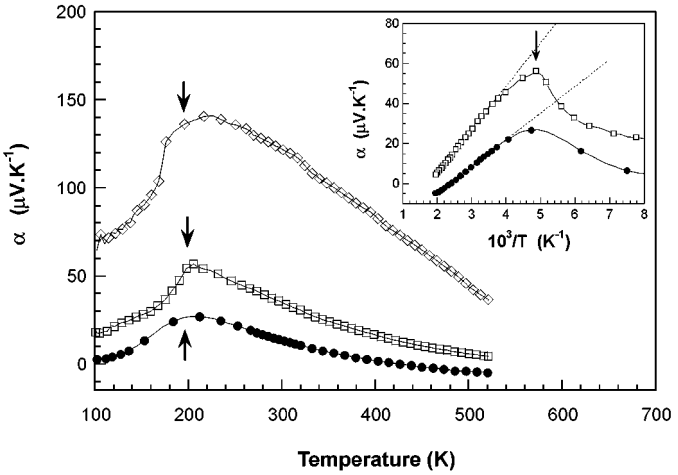

FIG. 6. Seebeck coefficient α as a function of temperature for $LaMnO_{3+\delta}$ samples with $\delta = 0.05$ (open diamonds), 0.15 (open squares), and 0.21 (solid circles). Arrows indicate the onset of ferromagnetic order, i.e., the temperature below which the magnetization starts increasing. In the inset, α is presented as a function of $1000/T$, the dotted lines correspond to fits using Eq. [3].

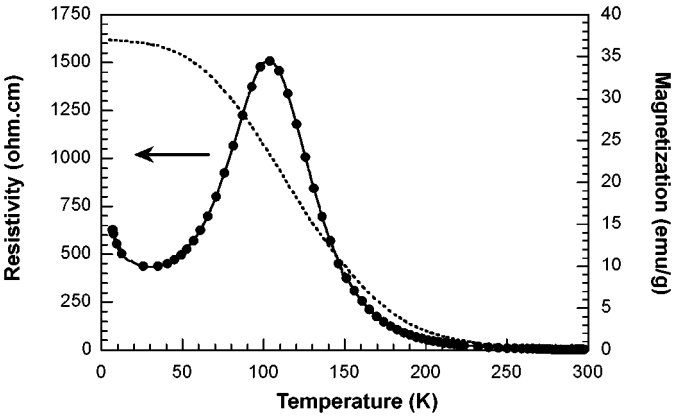

FIG. 7. Resistivity and magnetization as a function of temperature for a $LaMnO_{3.21}$ sample. The magnetization corresponds to a field-cooled measurement under 1000 Oe. The broadening of the transitions must be ascribed to the granularity of the material. Similar effects have been observed in $(La_{0.67}Ca_{0.33})MnO_{3+\delta}$ samples synthesized at low temperature and showing low vacancy contents: $\delta < 0.05$.

Fig. 6, dotted lines):

$$\alpha(T) = \frac{1}{e}\frac{E_S}{T} + \alpha_{spin}. \qquad [3]$$

The temperature-independent term, α_{spin} is ascribed to the degeneracy of the spin configuration (35, 36). For the vacancy-doped series, a calculation of the configurational entropy leads to $\alpha_{spin} = -42.3\ \mu V.K^{-1}$. The calculation is developed in the Appendix (37).

By analogy with semiconductors, E_S represents the ionization energy of the dopant, substituent, or vacancy (38). Alternatively, if we assume a polaronic-type transport, E_S can be assigned to the activation energy of the polaron density, that is to say, the energy difference between the Fermi level and the polaronic states (39). In any case, E_S gives a direct insight into the charge-carrier density. For all the compositions studied in this work, a positive sign of E_S confirms a *p*-type conductivity. The abrupt decrease of α below the onset of ferromagnetic order, in Fig. 6, accounts for both the suppression of the term related to the spin configuration entropy and a charge-carrier delocalization associated with the insulator-to-metal transition (see resistivity and magnetization vs temperature in Fig. 7).

The variation of E_S as a function of the Mn valence state is shown in Fig. 8a. We have compiled various literature data in addition to ours in order to get a general trend, using Refs. (33) and (34) for the Ca-doped series and Refs. (11) and (12) for the self-doped system. For the latter, E_S was calculated from the values of α at 250 and 300 K using Eq. [3]. E_S decreases upon doping and little difference is found between the two series. In the $LaMnO_{3+\delta}$ system, the progressive shift as compared to the aliovalent-doped samples, observed at high Mn(IV) contents ($\delta > 0.15$), can be simply related to the trapping of the excess holes as concluded from the XAS and XRD analyses.

Assuming that both the number of carriers and their mobility are thermally activated processes, the activation energy of the resistivity, E_ρ, can be described as the sum of two terms:

$$E_\rho = E_S + E_\mu. \qquad [4]$$

The quantity E_ρ is extracted from resistivity measurements in the paramagnetic regime using an adiabatic polaron hopping mechanism:

$$\rho(T) = \rho_0 T e^{E_\rho/k_B T}. \qquad [5]$$

Then E_μ represents the energy barrier for a hole jump between two Mn sites. Herein, the existence of a nonzero E_μ (see Table 3) is in good agreement with a polaronic transport (40). In the two systems, Ca- and self-doped, and for all doping levels, E_S is nearly one order of magnitude lower than the activation energy of the resistivity (Figs. 8a and 8b). This indicates that, in these perovskite oxides, mobility effects dominate the transport.

The activation energy, E_ρ, in the high-temperature regime is plotted as a function of the formal Mn(IV) content in Fig. 8b. In the Ca-doped series, E_ρ gradually decreases upon substitution, in relationship with the decrease in Mn–O bond length and hence with the increase of the band width. In contrast, in the self-doped system, this energy barely

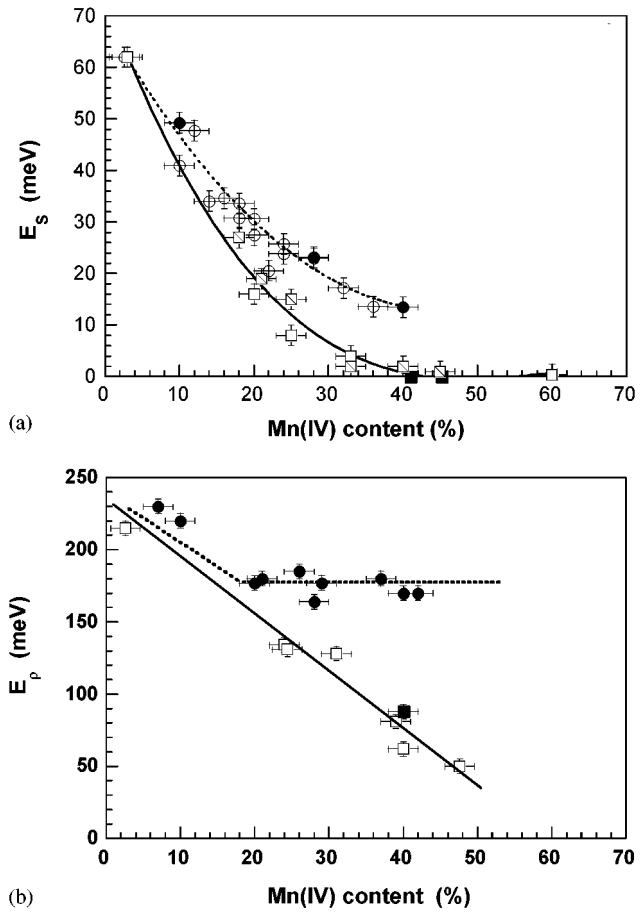

FIG. 8. (a) Activation energy of the charge-carrier density, E_S, as a function of the formal Mn(IV) content in the two series, $(La_{1-x}Ca_x)MnO_3$ and $LaMnO_{3+\delta}$. E_S was determined from Seebeck measurements in the paramagnetic regime using Eq. [3]. Solid symbols correspond to this work. Open symbols are reported from Refs. (11) and (12) (circles) for the self-doped series and from Refs. (33) (squares) and (34) (squares with diagonals) for the Ca-doped system. The $LaMnO_{3+\delta}$ literature data are calculated from α values at 250 and 300 K using Eq. [3]. The circles (resp. squares) are affected by the vacancy (resp. calcium)-doped systems. (b) Activation energy of the resistivity, E_ρ, in the paramagnetic regime as a function of the formal Mn(IV) content for the two systems. The circles (resp. squares) are affected by the vacancy (resp. calcium)-doped series. Solid symbols correspond to this work. Open symbols are derived from Ref. (33). Lines are just guides for the eyes.

changes upon doping and remains above a limit value of 170 meV. One should first remember that the activation energy for resistivity presents, in ceramic materials, a contribution related to microstructure effects and conduction across grain boundaries. However, we have estimated this contribution in the $(La_{1-x}Ca_x)MnO_3$ series for $x = 0.3$ and 0.4 and found that the increase in E_ρ is limited to 10–40 meV when the grain size is decreased from 10 to 25 nm. In particular, the activation process in samples synthesized above 900°C is almost not affected by the microstructure. This latter synthesis temperature corresponds to a δ value of 0.15 in the $LaMnO_{3+\delta}$ system. Since the energy assigned to the creation of mobile carriers (E_s) can be neglected in the case of highly doped samples (Fig. 8a), the large values of E_ρ in the $LaMnO_{3+\delta}$ series indicate a decrease of the hole mobility. Then E_μ probably accounts for an energy barrier due to a strong charge-carrier scattering by the ionic defects. Therefore, carriers show a much more localized character in the vacancy-doped series than in the aliovalent-doped systems, as already suggested by Mahendiran *et al.* from the analysis of TEP data in the low-temperature regime (41). As a consequence, trapping of the holes in excess of $\delta = 0.15$ in granular $LaMnO_{3+\delta}$ samples results from combined surface disorder effects and reduced carrier mobility.

Magnetic and Transport Properties

The occurrence of trapped holes in the self-doped system has led us to reconsider its electronic phase diagram. This diagram, based on our samples and literature data (11, 12, 14), is basically similar to that reported for all the aliovalent-doped manganite systems (42, 43): i.e., the antiferromagnetic insulator $LaMnO_3$ changes into a metallic ferromagnet upon doping (Fig. 9). In the vacancy-doped system, we have observed that a hole doping first induces an increase of the saturation magnetization, M_{sat}, up to its spin-only value (Table 3). Below 20% of Mn(IV), residual antiferromagnetic (AFM) correlations that may correspond either to the segregation of ferromagnetic clusters in an antiferromagnetic matrix or to a canted magnetic structure are present. A pure ferromagnetic (FM) character is then detected, as in the case of the Ca-doped samples. For this latter system, M_{sat}, strongly decreases above 40% of Mn(IV) and an antiferromagnetic ground state stands for higher hole contents.

However, although ferromagnetism and metallicity appear quasi-simultaneously in the $(La_{1-x}Ca_x)MnO_3$ system for $x \sim 0.18$, Fig. 9 shows the persistence of a low-temperature insulating regime over a wide range of compositions for the $LaMnO_{3+\delta}$ samples. Thus, the self-doped system presents an unusual ferromagnetic-insulating (FMI) ground state for an extended range of compositions: $0.10 \leq \delta \leq 0.15$. This FMI regime demonstrates that hole delocalization over long distances is not a prerequisite for establishing a ferromagnetic long-range order. A low-temperature metallic behavior only appears at high hole contents, $\delta > 0.15$, as shown for the $LaMnO_{3.21}$ sample (Fig. 7).

In the Ca- and vacancy-doped series, the different extent of the insulating compositions can be discussed in terms of charge-carrier density and/or mobility. In both systems, for doping levels below 30%, the point defects are all ionized and holes are uniformly distributed over the lattice, as

TABLE 3

Formal Mn(IV) Content, Saturation Magnetization M_{sat} and Value Expected for a Full Spin Alignment M_{theo}, and Activation Energy of the Charge-Carrier Density E_S and of the Resistivity E_ρ Measured in the Paramagnetic Regime for the $LaMnO_{3+\delta}$ samples ($0.03 \leq \delta \leq 0.21$)

$LaMnO_{3+\delta}$ δ	Mn(IV) content (%)	M_{sat} (μO_B/Mn)	M_{theo} (μ_B/Mn)	T_C (K)	T_ρ (K)	E_S (meV)	E_ρ (meV)	E_μ (meV)
0.03	7±2	0.724±0.007	3.93±0.02	150	—		227±5	
0.05	10±2	1.41±0.04	3.89±0.02	170	—	49±2	220±5	171±7
0.07	15±2	3.63±0.04	3.85±0.02	155	n	n	n	n
0.09	19±2	3.77±0.04	3.81±0.02	170	—		177±5	
0.10	21±2	3.73±0.04	3.79±0.02	170	—		180±5	
0.13	26±2	3.50±0.04	3.74±0.02	150	—		185±5	
0.15	30±2	3.62±0.04	3.70±0.02	150	—	23±2	177±5	154±7
0.19	38±2	2.64±0.04	3.62±0.02	125	103		171±5	
0.21	42±2	2.40±0.04	3.58±0.02	145	109	14±2	170±5	156±7

Note. The saturation magnetization is affected by the grain size. In $(La_{0.67}Ca_{0.33})MnO_{3+\delta}$ samples synthesized between 700 and 1475°C and showing low vacancy concentration ($\delta < 0.05$), M_{sat} is strongly decreased for nanometric powder samples. n: not measured.

demonstrated by XANES spectroscopy. Analysis of the Seebeck coefficient in the paramagnetic regime also confirms that electrical conductivity is not limited by the number of carriers. However, a large scattering of these carriers by the bulk vacancies drastically decreases their mobility, as shown by the persistence of large E_μ values in the $LaMnO_{3+\delta}$ system. This reduced mobility explains that an insulator-type behavior is maintained in the ferromagnetic regime for $0.1 \leq \delta \leq 0.15$.

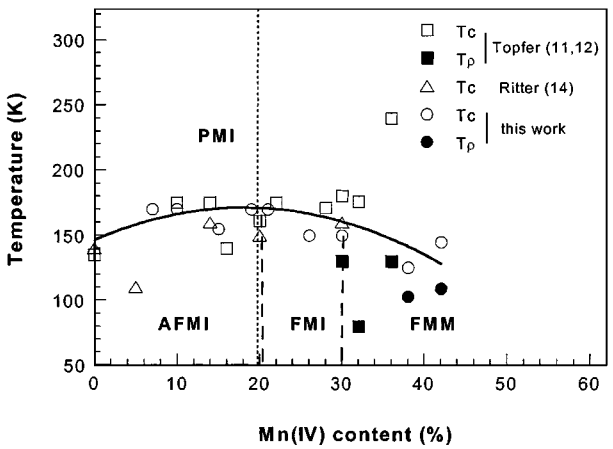

FIG. 9. Electronic phase diagram for the $LaMnO_{3+\delta}$ system, based on the present work (○, T_C; ●, T_ρ) and literature data (11, 12; □, T_C; ■, T_ρ) and (14; △, T_C). Above 30% of Mn(IV), the discrepancy between Curie temperatures may originate from the way of defining T_C from magnetization measurements (inflection point of $M(T)$) or susceptibility data (onset of divergence of the susceptibility). In the Ca-doped series, the transition between the insulating and the metallic regimes is observed around 18% as indicated by the dotted line (42). The abbreviations correspond to paramagnetic insulator (PMI), antiferromagnetic insulator (AFMI), ferromagnetic insulator (FMI), and ferromagnetic metal (FMM).

Finally, the occurrence of a low-temperature metal-like conductivity for the $LaMnO_{3.20\pm0.01}$ compositions remains intriguing (Figs. 7 and 9). Paradoxically, a metallic behavior is only observed in samples in which the holes in excess of the 30% limit appear trapped at the surface of the grains, as evidenced by XAS experiments performed at 300 and at 80 K in the FM regime. However, as these samples are formed of nanoparticles (of 25 nm in diameter), this unexplained result may originate from the small grain size that favors an interference between the surface defect states and the conduction band.

CONCLUSIONS

Doping the $LaMnO_3$ perovskite through aliovalent substitution or cationic vacancy insertion induces both a decrease of the unit cell volume and a gradual shift of the Mn *K*-edge absorption to high energies. Both trends account for an increasing hole density in the Mn 3*d* band. However, in the $LaMnO_{3+\delta}$ system, the lattice volume shows a deviation from this linear variation above 30% of Mn(IV), which corresponds to a limit of solubility for pairs of La and Mn vacancies. A thorough analysis of the XAS spectra indicates that this discontinuity arises from a hole localization on Mn sites, presumably on Mn surface sites. Above this solubility limit, the unit cell volume remains nearly constant and the shape of the absorption lines indicates increasing amounts of trapped holes. Electrostatic interactions with the ionic defects, which reduce the hole mobility, in conjunction with surface disorder effects lead to this localization process.

The $LaMnO_{3+\delta}$ system shows the persistence of a low-temperature insulating ground state at high hole-doping levels, even in the ferromagnetic regime: $0.10 \leq \delta \leq 0.15$.

The activation energy of the charge-carrier density, determined through Seebeck measurements, and the analysis of the Mn K-edge absorption show that this insulating character does not come from a reduced concentration of mobile carriers. This ferromagnetic-insulating state rather accounts for a decrease of the carrier mobility, as evidenced by the combined resistivity and Seebeck data. Finally, the occurrence of a low-temperature metal-like conductivity in $LaMnO_{3.20\pm0.01}$ samples remains unexplained. Such an insulator-to-metal transition in the ferromagnetic regime, while the number of mobile carriers remains constant, may be attributed to an increase of the hole mobility associated with an overlap between the conduction band and the defect states.

APPENDIX

For all the manganite systems, the Seebeck coefficient, α at high temperature can be assimilated to the entropy per charge-carrier:

$$\alpha_{T\to\infty} = \frac{1}{e}\left(\frac{\partial S}{\partial p}\right).$$

Here, the entropy S is related to the degeneracy of the spin configuration: $S = k_B \ln \Omega$ with $\Omega = (2\sigma_1 + 1)^{n_1}(2\sigma_0 + 1)^{n_0}$. n_1 (resp. n_0) corresponds to the number of Mn^{4+} (resp. Mn^{3+}) ions. $\sigma_1 = \frac{3}{2}$ (total spin of Mn^{4+}, $3d^3$) and $\sigma_0 = 2$ (total spin of Mn^{3+}, $3d^4$). For $La_{3/(3+\delta)}Mn_{3/(3+\delta)}O_3$ compositions, the number of Mn^{4+} species is

$$n_1 = \frac{3N}{3+\delta}\,2\delta = p,$$

where N is the number of Mn sites, occupied or not. The number of Mn^{3+} ions is then

$$n_0 = \frac{3N}{3+\delta}(1-2\delta) = N - \frac{7}{6}\,p.$$

Hence,

$$\alpha_{spin} = \frac{k_B}{e}\ln\frac{(2\sigma_1+1)}{(2\sigma_0+1)^{7/6}} = -42.3\ \mu V.K^{-1}.$$

Note that, for the $(La_{1-x}Ca_x)MnO_3$ system (33, 34),

$$\alpha_{spin} = \frac{k_B}{e}\ln\frac{(2\sigma_1+1)}{(2\sigma_0+1)} = -19.2\ \mu V.K^{-1}.$$

ACKNOWLEDGMENTS

The authors thank P. Berthet and A. Revcolevschi, Laboratoire de Physico-Chimie des Solides d'Orsay, and Jean Etourneau, Institut de Chimie de la Matière Condensée de Bordeaux, for helpful discussions. E. Marquestaut is also acknowledged for assistance during the Seebeck experiments. The authors are grateful to the LURE for the provision of X-ray beam time.

REFERENCES

1. R. J. H. Voorhoeve, "Advanced Materials in Catalysis." Academic Press, New York, 1977.
2. R. von Helmolt, J. Wecker, B. Holzapfel, L. Schultz, and K. Samwer, *Phys. Rev. Lett.* **71,** 2331–2333 (1993).
3. K. Chahara, T. Ohno, M. Kasai, and Y. Kozono, *Appl. Phys. Lett.* **63,** 1990–1992 (1993).
4. J. Volger, *Physica* **20,** 49–66 (1954).
5. C. Zener, *Phys. Rev.* **82,** 403–405 (1951).
6. B. C. Tofield and W. R. Scott, *J. Solid State Chem.* **10,** 183–194 (1974).
7. J. A. M. van Roosmalen, E. H. P. Cordfunke, R. B. Helmholdt, and H. W. Zandbergen, *J. Solid State Chem.* **110,** 100–105 (1994).
8. J. A. M. van Roosmalen and E. H. P. Cordfunke, *J. Solid State Chem.* **110,** 106–108 (1994).
9. J. M. Tranquada, S. M. Heald, A. R. Moodenbaugh, and Y. Xu, *Phys. Rev. B* **38,** 8893–8899 (1988).
10. J. A. M. van Roosmalen and E. H. P. Cordfunke, *J. Solid State Chem.* **110,** 109–112 (1994).
11. J. Töpfer, J.-P. Doumerc, and J.-C. Grenier, *J. Mater. Chem.* **6,** 1511–1516 (1996).
12. J. Töpfer and J. B. Goodenough, *J. Solid State Chem.* **130,** 117–128 (1997).
13. B. C. Hauback, H. Fjellvag, and N. Sakai, *J. Solid State Chem.* **124,** 43–51 (1996).
14. C. Ritter, M. R. Ibarra, J. M. De Teresa, P. A. Algarabel, C. Marquina, J. Blasco, J. Garcia, S. Oseroff, and S. W. Cheong, *Phys. Rev. B* **56,** 8902–8911 (1997).
15. I. O. Troyanchuck, H. Szymczak, N. V. Kasper, and A. Nabialek, *J. Solid State Chem.* **130,** 171–175 (1997).
16. J. A. Alonso, M. J. Martinez-Lope, M. T. Casais, and A. Munoz, *Solid State Comm.* **102,** 7–12 (1997).
17. M. Verelst, N. Rangavittal, C. N. R. Rao, and A. Rousset, *J. Solid State Chem.* **104,** 74–80 (1993).
18. R. Mahesh, K. R. Kannan, and C. N. R. Rao, *J. Solid State Chem.* **114,** 294–296 (1995).
19. R. D. Shannon and C. T. Prewitt, *Acta Crystallogr. Sect. A* **32,** 785 (1976).
20. I. Maurin, P. Barboux, Y. Lassailly, and J.-P. Boilot, *Chem. Mat.* **10,** 1727–1732 (1998).
21. I. Maurin, P. Barboux, Y. Lassailly, J.-P. Boilot, and F. Villain, *J. Magn. Magn. Mater.* **211,** 139–144 (2000).
22. P. Dordor, E. Marquestaut, and G. Villeneuve, *Rev. Phys. Appl.* **15,** 1607–1612 (1980).
23. Q. Huang, A. Santoro, J. W. Lynn, R. W. Erwin, J. A. Borchers, J. L. Peng, K. Ghosh, and R. L. Greene, *Phys. Rev. B* **58,** 2684–2691 (1998). S. Faaland, K. D. Knudsen, M. A. Einarsrud, L. Rormark, R. Hoier, and T. Grande, *J. Solid State Chem.* **140,** 320–330 (1998).
24. H. Y. Hwang, S. W. Cheong, P. G. Radaelli, M. Marezio, and B. Batlogg, *Phys. Rev. Lett.* **75,** 914–917 (1995).
25. R. Mahendiran, S. K. Tiwary, A. K. Raychaudhuri, T. V. Ramakhrishnan, R. Mahesh, N. Rangavittal, and C. N. R. Rao, *Phys. Rev. B* **53,** 3348–3358 (1996).
26. J. Töpfer and J. B. Goodenough, *Chem. Mat.* **9,** 1467–1474 (1997).
27. J. A. M. van Roosmalen, P. van Vlaanderen, E. H. P. Cordfunke, W. L. Idjo, and D. J. W. Idjo, *J. Solid State Chem.* **114,** 516–523 (1995).

28. A. Manceau, A. I. Gorshkov, and V. A. Drits, *Am. Miner.* **77,** 1133–1143 (1992).
29. M. Croft, D. Sills, M. Greenblatt, C. Lee, S. W. Cheong, K. V. Ramanujachary, and D. Tran, *Phys. Rev. B* **55,** 8726–8732 (1997).
30. O. Toulemonde, F. Studer, A. Barnabe, A Maignan, C. Martin, and B. Raveau, *Eur. Phys. J. B* **4,** 159–167 (1998).
31. G. Subias, J. Garcia, M. G. Proietti, and J. Blasco, *Phys. Rev. B* **56,** 8183–8191 (1997).
32. C. H. Booth, F. Bridges, G. H. Kwei, J. M. Lawrence, A. L. Cornelius, and J. J. Neumeier, *Phys. Rev. B* **57,** 10,440–10,453 (1998).
33. M. F. Hundley and J. J. Neumeier, *Phys. Rev. B* **55,** 11,511–11,515 (1997).
34. T. T. M. Palstra, A. P. Ramirez, S. W. Cheong, B. R. Zegarski, P. Schiffer, and J. Zaanen, *Phys. Rev. B* **56,** 5104–5107 (1997).
35. P. M. Chaikin and G. Beni, *Phys. Rev. B* **13,** 647–651 (1976).
36. J.-P. Doumerc, *J. Solid State Chem.* **110,** 419–420 (1994).
37. I. Maurin, thesis, Ecole Polytechnique (2000).
38. J. M. Ziman, "Electrons, and Phonons," Oxford Univ. Press, Oxford, 1972.
39. D. Emin, *Phys. Rev. Lett.* **35,** 882–885 (1975).
40. H. Reik, *in* "Polarons in Ionic Crystals and Polar Semiconductors" (J. T. Devreese, Ed.), pp. 679–714. North-Holland, Amsterdam, 1972.
41. R. Mahendiran, S. K. Tiwary, A. K. Raychaudhuri, R. Mahesh, and C. N. R. Rao, *Phys. Rev. B* **54,** 9604–9607 (1996).
42. P. Schiffer, A. P. Ramirez, W. Bao, and S. W. Cheong, *Phys. Rev. Lett.* **75,** 3336–3339 (1995).
43. T. Boix, F. Sapina, Z. El-Fadli, E. Martinez, and A. Beltran, *Chem. Mater.* **10,** 1569–1575 (1998).